Ice fabrics in natural flows: beyond pure and simple shear

Daniel H. M. Richards[1], Samuel S. Pegler[2], and Sandra Piazolo[3]

[1]Fluid Dynamics CDT, University of Leeds, United Kingdom
[2]School of Mathematics, University of Leeds, United Kingdom
[3]School of Earth and Environment, University of Leeds, United Kingdom

Correspondence: Daniel H. M. Richards (scdhmr@leeds.ac.uk)

Abstract. Ice fabrics are key for understanding and predicting ice flow dynamics. Despite its importance, the characteristics and evolution of ice fabrics beyond pure and simple shear flow has largely been neglected. However, 80% of the flow of ice in Antarctica is outside the regimes of pure and simple shear. We use a new validated numerical model (SpecCAF), which has been shown to accurately reproduce experimentally observed fabrics in both compression and simple shear, to explore the fabrics produced between pure and simple shear, as well as those that are highly rotational. We present a definitive classification of all fabric patterns. We find that intermediate deformations between pure and simple shear result in a smooth transition between a fabric characterised by a cone-shape and a secondary cluster pattern. Highly-rotational fabrics are found to produce a weak girdle fabric. In addition we obtain complete predictions for the strain required for any fabric under a 2D deformation to reach steady state at any given temperature. Use of our data in current ice flow models as well as for ice core fabric and seismic anisotropy interpretation will enhance the communities' ability to predict future ice flow in a changing climate.

1 Introduction

Mass loss from ice sheets is set to be the main contributor to sea-level rise this century (e.g. Shepherd et al., 2018). Reliably predicting sea-level rise depends on accurately modelling ice flow. One of the most important controls on ice flow dynamics is the ice fabric, i.e. the arrangement of ice grains in terms of their crystallographic axes. Strong alignment of the crystal lattices may cause the strain-rate response to an applied stress to vary by a factor of 9 in different directions (e.g. Pimienta and Duval, 1987). Hence, understanding the fabrics present in any flowing ice sheet, i.e. Antarctica or Greenland, is important for predicting ice-sheet flow and, in turn, the loss of ice over time.

There are a number of issues that need to be resolved before it is possible to fully interpret ice fabrics from ice cores and to be able to predict future ice flow taking ice fabric effects into account. Firstly, it is unknown what deformations are important in the natural world, for example the Antarctic ice-sheet. Secondly, if deformation regimes that have not been studied in experiments are common in the natural world, what fabrics are produced from these deformations? It is also unknown how fabrics evolve at very high strains which cannot be explored in experiments. Furthermore, at these high strains, how is the final steady-state dependent on parameters such as temperature and type of deformation, and can it be reached in the natural world? By exploring the predictions of a recently developed experimentally constrained continuum model for ice fabrics (Richards et al., 2021), we will address each of these questions.

2 Background

2.1 Fabric Development

2.1.1 Processes governing fabric development

The distribution of crystallographic orientations within a polycrystal is called the fabric or crystallographic preferred orientation
30 (CPO). Due to the dominance of basal slip in ice (Duval et al., 1983), it is sufficient to consider the orientation changes
through time of the normal to the basal plane, referred to as the c-axis, alone. As ice flows, the c-axes align to produce a
fabric from the combination of deformation and recrystallization. There are four main processes which affect the fabric: basal-
slip deformation, migration recrystallization, rigid-body rotation and rotational recrystallization. Basal-slip deformation can
be understood through the analogy of a deck of cards sliding over one another causing c-axes to rotate towards the axis of
35 compression (Azuma and Higashi, 1984; van der Veen and Whillans, 1994). Migration recrystallization is the process whereby
grains with a lower dislocation density grow into neighbouring grains with higher dislocation density. The dislocation density
at a specific grain is primarily caused by the stress imposed on the grain, which is dependent on the orientation of that grain
relative to the deformation. As a consequence of the stress on the grain, dislocations appear and grow. Depending on the
deformation, grains at certain orientations will grow at the expense of others. Therefore the effect of migration recrystallization
40 is to produce c-axes clustered towards certain orientations in the polycrystal. Rotational recrystallization occurs where sub-
grains form close to the grain boundaries due to localised stress concentrations (Drury and Urai, 1990). This acts to diffuse any
concentrations of c-axis towards a particular orientation (Gödert, 2003). Rigid-body rotation acts to rotate any c-axes according
to the rotational characteristics of the deformation regime the ice grains are subjected to.

2.1.2 Observed fabrics

45 Ice fabrics can be observed through laboratory experiments, the taking of ice cores from real-world locations, and more recently
inferred through seismic measurements.

In the laboratory, the majority of experiments are performed in compression, either in pure shear (2D) or unconfined com-
pression (3D), without any rotational component (Jacka and Maccagnan, 1984; Jacka, 2000; Craw et al., 2018; Fan et al., 2020;
Piazolo et al., 2013) and others. The other end-member is simple-shear (Journaux et al., 2019; Qi et al., 2019). Wilson and
50 Peternell (2012) is the only work exploring intermediate deformations, focusing mainly on the stain-rate response. Laboratory
experiments provide detailed fabric measurements in known conditions. However experiments are limited to strains of around
0.4 for compression (Fan et al., 2020) and 2 for direct simple shear (Qi et al., 2019).

Analysis of fabrics can also be done by taking ice cores in real world locations. Initial studies of ice cores have concentrated
on ice domes or divides (Gow, 1961; Holtzscherer et al., 1954; Johnsen et al., 1995). These locations are deliberately chosen
55 because they have minimal deformation, to act as a good proxy for past climate data. At domes, the ice will be deformed
vertically in unconfined compression, producing either a single-maximum or a girdle shape fabric, as shown in Fig. 1. Recently,
ice cores have become available in locations with more complex deformation histories (Stoll, 2019; Treverrow et al., 2010).

Figure 1. Illustration showing common fabrics or CPOs which develop in ice, illustrated by their pole figures, as well as the deformation and temperature they typically occur at. The pole figures show the distribution of c-axis orientations, with the compression axis at the centre. (a) shows a single-maximum fabric, produced in unconfined compression or simple shear at low temperatures (Qi et al., 2019). (b) shows a cone-shape fabric, produced in unconfined compression at higher temperatures, when grain-boundary migration is active (Paterson, 1999). This can also be considered a girdle fabric when the cone-angle approaches $90°$. (c) shows a double maxima fabric produced in confined compression (pure shear). (d) shows a single-maximum with a secondary cluster, produced in simple shear at higher temperatures (Qi et al., 2019).

Stoll (2019) show examples of a variety of fabric shapes such as girdles and single-maximum fabrics orientated in different directions as well as relatively faster fabric development with depth compared to ice cores at domes. An understanding of the fabrics produced in different conditions could enable us to better understand the deformation and temperature history of ice cores. Fabrics can also be measured from boreholes using more recent sonic and optical measurements (Kluskiewicz et al., 2017; Rongen et al., 2020).

Recently, data from radar and seismics has also been used to infer fabric properties (Matsuoka et al., 2003; Fujita et al., 2006; Booth et al., 2020). These methods can capture natural ice fabrics without expensive drilling, allowing data to be collected at more active locations such as ice streams (Jordan et al., 2020).

2.1.3 Fabric patterns

Figure 1 shows some commonly observed CPO patterns seen in experiments and from ice cores. These are illustrated by pole figures which show half of the of c-axis orientations (which cover the space of a unit sphere) projected onto a plane. As the c-axes are antipodally symmetric this is sufficient to show all the information. Laboratory experiments studying CPO evolution have been performed mostly in uniaxial compression and this produces either a single maximum at low temperatures (Fig. 1a) or a cone-shape fabric at high temperatures (Fig. 1b). At low temperature basal-slip deformation dominates and this causes c-axes to rotate towards the axis of compression, producing the single-maximum in Fig. 1a. The cone-shape fabric in Fig. 1b is produced by the balance of basal-slip deformation and migration recrystallization. The process of migration recrystallization acts to consume grains orientated towards the compression axis, and grow grains orientated in a ring $45°$ away from the compression axis. Therefore, the balance of basal-slip deformation and migration recrystallization produces a ring or cone-shape pattern in the pole figure. In pure shear, which is a 2D compression, the grains produced by migration recrystallization

do not form a ring but rather two clusters at $45°$, hence the double-maxima fabric in Fig. 1c is produced rather than a cone-shape fabric.

Recent simple shear experiments produce either a single-maximum at low temperatures, or a single-maximum with an offset secondary cluster (Fig. 1d) at intermediate strains and high temperatures (Qi et al., 2019; Journaux et al., 2019). This pattern is similar to a double-maxima but the presence of vorticity in simple shear deformations causes the cluster not aligned with the shear plane normal to be advected towards the primary cluster. As the secondary cluster's orientation changes, grains of that orientation accumulate more dislocations so start to be consumed by migration recrystallization. This results in the imbalance in cluster strengths seen in Fig. 1d.

2.2 Flow regimes

2.2.1 General deformations

There exist a significant variety of deformations in the natural world. One way to classify a deformation is by the vorticity number (Passchier, 1991), which measures the ratio of vorticity magnitude to shearing magnitude:

$$\mathcal{W} = \sqrt{\frac{W_{ij}W_{ij}}{D_{ij}D_{ij}}}, \tag{1}$$

where $\mathbf{W} = \frac{1}{2}(\nabla \boldsymbol{u} - \nabla \boldsymbol{u}^T)$ is the anti-symmetric part of the velocity gradient (the spin-rate tensor) and $\mathbf{D} = \frac{1}{2}(\nabla \boldsymbol{u} + \nabla \boldsymbol{u}^T)$ is the symmetric part of the velocity gradient (the strain-rate tensor). Figure 2 illustrates different flow regimes and the corresponding vorticity number $\mathcal{W}$ for each. The vorticity number is 0 for pure shear or uniaxial compression, 1 for simple shear and ∞ for rigid-body rotation. Ice in the natural world will experience deformations with vorticity numbers from 0 to ∞, however to date fabrics produced for $\mathcal{W} = 0$ and $\mathcal{W} = 1$ are the only areas which have been extensively explored due to the limitations of possible deformations in experiments.

In geology, numerous studies have shown that in the natural world the full range of different deformation regimes occur (Jiang, 1994; Bailey and Eyster, 2003). Such studies have been supported by theoretical (Fossen and Tikoff, 1993; Tikoff and Fossen, 1995) and analogue modelling (Piazolo et al., 2002, 2004), (ten Grotenhuis et al., 2002).

2.2.2 Deformations in the natural world

By an analogy to geology (Beam and Fisher, 1999; Xypolias, 2010) we expect a variety of deformations are likely to occur in natural ice flow. To test this hypothesis, we have used surface velocity data from Antarctica (Mouginot et al., 2019) to calculate the surface vorticity number, shown in Fig. 3. To reduce the errors in the data we have taken the mean value from a 10×10 block (covering a 4.5 km square). We have defined the standard deviation of any variables, such as velocity components, as the variance from the mean of the 100 samples in each 10×10 block. The relative standard deviation controls the transparency: if this is $> 100\%$ this location is plotted as white, and a relative standard deviation of 0% is plotted as the full colour. From this figure we can see that there are many regions of Antarctica where the surface vorticity number is both at intermediate values
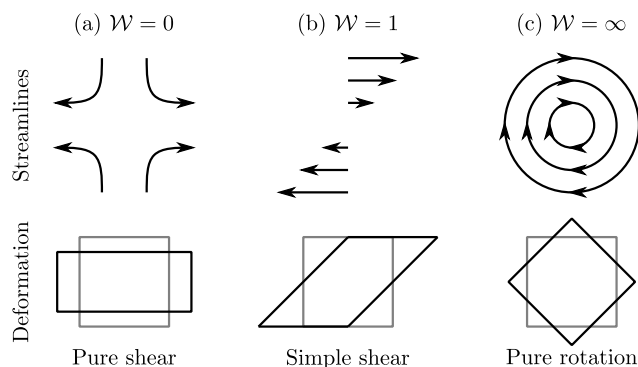
Figure 2. Schematic illustrating flow regimes at different vorticity numbers $\mathcal{W}$ (Eq. (1)): (a) Pure shear ($\mathcal{W} = 0$), (b) Simple shear ($\mathcal{W} = 1$), (c) Pure rotation ($\mathcal{W} = \infty$). For each flow regime the streamlines and deformation produced are shown. In experiments only pure and simple shear have been considered extensively.

between 0 and 1, and many areas where $\mathcal{W} > 1$. The regions characterised by high vorticity numbers ($\mathcal{W} > 1$) typically shown to occur in the regions of ice streams with curved streamlines.

Figure 4a shows a cumulative distribution plot of the surface vorticity numbers present in Fig. 3 and Fig. 4b shows the corresponding distribution plot (the derivative of 4a). Both plots highlight the difference in the distribution between all velocity magnitudes, and the fastest and slowest 5%. From this we can see that intermediate deformations ($0.1 < \mathcal{W} < 0.9$) are very common, accounting for around 70% of the deformations. Figure 4b shows that slow speeds are dominated by vorticity numbers close to 0.4, i.e. with a significant pure shear component. This is contrasted by the fastest 5% which are dominated by simple shear ($\mathcal{W} = 1$). Highly rotational regions ($\mathcal{W} > \infty$) are also important, as they are common in the fastest regions: 40% of the deformations with the fastest 5% of speeds have $\mathcal{W} > 1$.

2.3 Modelling ice fabrics

There are currently several approaches for modelling ice fabrics. Some approaches model the microstructure directly (Llorens et al., 2016; Kennedy and Pettit, 2015). This involves simulating grain-grain interactions and imposes deformation as a boundary condition. This is useful for improving our understanding of ice microstructure and fabric evolution but is numerically expensive. At the other end of the scale, models such as presented by Gillet-Chaulet et al. (2005) track the evolution of tensorial descriptions of the fabric, without including migration recrystallization. These cannot accurately reproduce detailed fabric patterns but are computationally cheap enough for integration into large-scale models (Gagliardini et al., 2013).

Placidi et al. (2010) developed a continuum model including all relevant processes (see section 2.1.1). This was recently accurately solved using a spectral method and constrained against experiments by Richards et al. (2021). This model (SpecCAF) has been shown to predict fabrics accurately with only temperature and deformation as inputs. SpecCAF reproduces fabrics from experiments performed in compression and simple shear.
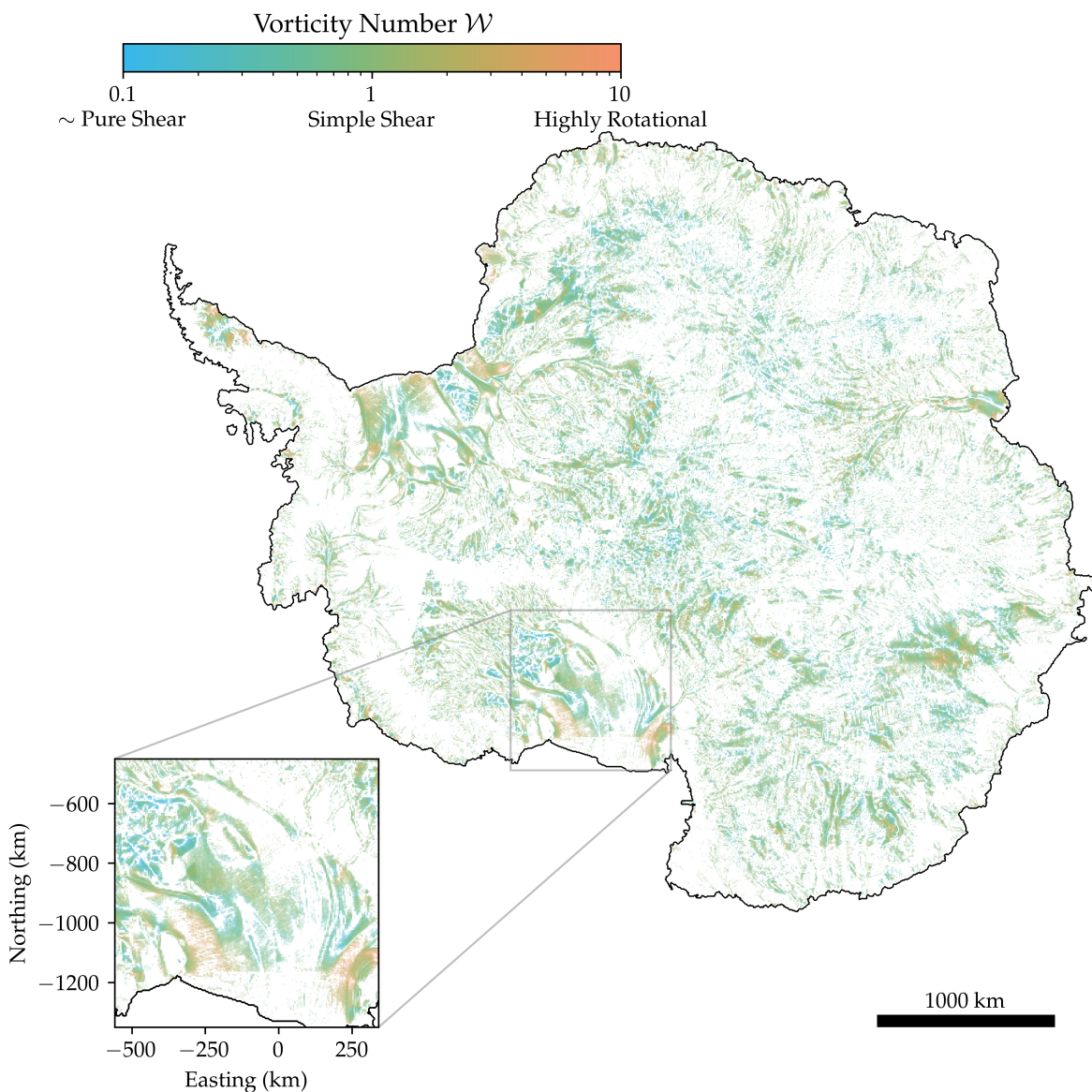
Figure 3. Vorticity number (defined in Eq. (1)) calculated from the surface velocity data of Antarctica (Mouginot et al., 2019) after averaging over a 10×10 block and taking the mean value within each block. The colour shows the vorticity number on a log scale. The transparency shows the relative error: an error in $\mathcal{W}$ of 100% or greater is plotted as white and an error of 0% is plotted as the full colour. The inset shows the Ross Ice Shelf, with the easting and northing in Antarctic polar stereographic coordinates. This figure shows considerable variation in vorticity number across the continent, including deformations not accessible in the laboratory (this result is also highlighted in Fig. 4).
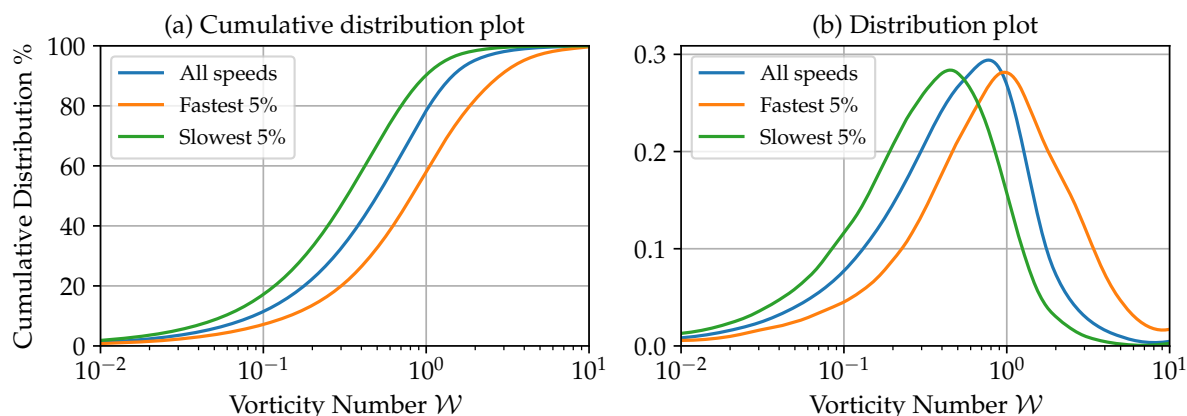
Figure 4. Distribution of surface vorticity numbers of Antarctica, shown in Fig. 3. (a) shows the cumulative distribution and (b) shows the derivative of this, the distribution plot. For both, the distribution is shown for all speeds, the fastest 5% ($|\boldsymbol{u}| > 404\,\mathrm{ma}^{-1}$) and the slowest 5% ($|\boldsymbol{u}| < 0.83\mathrm{ma}^{-1}$).

2.4 Open questions addressed here

In this paper we use the SpecCAF model to address several open questions. First, we determine for the fist time the evolution of fabrics in general 2D deformations, bridging the complete spectrum from pure shear to rigid-body rotation, across the range of
130 temperatures seen in ice sheets. We explore how fabric patterns evolve, and construct a complete regime diagram documenting fabrics that arise over the space of temperature, deformation, and strain, and explain the physical balances leading to these fabrics. Finally, we present a complete assessment of steady-state properties of ice fabrics, such as fabric strength and finite strain required to reach steady state, across the space of deformation and temperature.

3 Methods

135 The SpecCAF model, following work by Placidi et al. (2010), uses a continuum approach to represent the mass distribution of *c*-axes within a polycrystal, termed the *orientation mass density*.

$$\rho(\boldsymbol{x},t) = \int_{S^2} \rho^*(\boldsymbol{x},t,\boldsymbol{n})\,\mathrm{d}\boldsymbol{n}. \tag{2}$$

In this equation $\rho^*\mathrm{d}\boldsymbol{n}$ is the mass fraction of grains with orientations towards the unit orientation vector $\boldsymbol{n}$ within the solid angle $\mathrm{d}\boldsymbol{n}$. Therefore, integrating ρ^* over the space of possible orientations (the surface of a unit sphere S^2) gives the mass
140 density of ice at that particular point in physical space. The unit vector $\boldsymbol{n}$ is defined by two angles in spherical coordinates $\boldsymbol{n}(\theta,\varphi)$, representing any possible orientation. As we are modelling orientation evolution, the gradient operator is restricted so

only the two angles θ, φ (and not the length of the vector) change in spherical coordinates:

$$\nabla^* \boldsymbol{a}^* = \frac{\partial \boldsymbol{a}^*}{\partial \boldsymbol{n}} - \left(\frac{\partial \boldsymbol{a}^*}{\partial \boldsymbol{n}} \cdot \boldsymbol{n}\right) \boldsymbol{n} = \frac{\partial a_i^*}{\partial n_j} - \frac{\partial a_i^*}{\partial n_l} n_l n_j, \tag{3}$$

where $\boldsymbol{a}^*$ is an arbitrary vector in orientation space.

145   We model the evolution of the orientation mass density ρ^* defined in Eq. (2) under the effects of vorticity, basal-slip deformation, rotational and migration recrystallization, using the model first defined in Placidi et al. (2010):

$$\frac{\partial \rho^*}{\partial t} = -\nabla^* \cdot [\rho^* \boldsymbol{v}^*] + \lambda \nabla^{*2}(\rho^*) + \beta \left(\mathcal{D}^* - \langle \mathcal{D}^* \rangle\right) \rho^*. \tag{4}$$

The term $\boldsymbol{v}^*$ is the orientation transition rate, defined as:

$$v_i^* = W_{ij} n_j - \iota[D_{ij} n_j - n_i n_j n_k D_{jk}]. \tag{5}$$

150   The term $W_{ij} n_j$ in Eq. (5) represents the effect of vorticity on the CPO. The second term models basal-slip deformation. The non-dimensional parameter ι represents the ratio of basal-slip deformation to rigid-body rotation. Equation (5) was first used to describe the rotation of an individual ice grain (Svendsen and Hutter, 1996) but here it is used to describe a continuum. We refer the interested reader to Richards et al. (2021) for more details.

The term $\nabla^{*2}(\rho^*)$ models rotational recrystallization through a diffusion in orientation space (Gödert, 2003). The rate is

155   controlled by the parameter λ (s^{-1}). Migration recrystallization is modelled by the term $\left(\mathcal{D}^* - \langle \mathcal{D}^* \rangle\right) \rho^*$, which acts as an orientationally dependent source term. The deformability $\mathcal{D}^*$ is defined as

$$\mathcal{D}^* = 5 \frac{(D_{ij} n_j)(D_{ik} n_k) - (D_{ij} n_j n_i)^2}{D_{mn} D_{nm}}. \tag{6}$$

The parameter β (s^{-1}) controls the rate of migration modelled recrystallization. The average of $\mathcal{D}^*$ is defined as:

$$\langle \mathcal{D}^* \rangle = \int_{S^2} \frac{\rho^*}{\rho} \mathcal{D}^* \, \mathrm{d}\boldsymbol{n} \tag{7}$$

160   At a given orientation $\boldsymbol{n}$, if $\mathcal{D}^* > \langle \mathcal{D}^* \rangle$ then $\rho^*(\boldsymbol{n})$ will increase. This models grains growing or nucleating at this orientation due to migration recrystallization. This source term always conserves the integral of ρ^* over orientation space. The factor of 5 in Eq. (6) is a convention. The reader is referred to Placidi et al. (2010) or Richards et al. (2021) for a more detailed explanation.

3.1   Non-dimensionalisation

To apply Eq. (4) to spatially homogeneous fabrics and to compare to fabrics deformed in the laboratory we perform a non-

165   dimensionalisation as in Richards et al. (2021), where we non-dimensionalise by a characteristic density ρ_0 and effective strain-rate $\dot{\gamma}$. We represent non-dimensional variables with tildes and they are defined as:

$$\tilde{\rho}^* = \frac{\rho^*}{\rho_0}, \quad \tilde{\mathbf{D}} = \frac{\mathbf{D}}{\dot{\gamma}}, \quad \tilde{\mathbf{W}} = \frac{\mathbf{W}}{\dot{\gamma}}$$

$$\tilde{\lambda}(T, \dot{\gamma}) = \frac{\lambda(T, \dot{\gamma})}{\dot{\gamma}}, \quad \tilde{\beta}(T, \dot{\gamma}) = \frac{\beta(T, \dot{\gamma})}{\dot{\gamma}}.$$

As in Richards et al. (2021) this gives the non-dimensional form of Eq. (4):

$$\frac{\partial \tilde{\rho}^*}{\partial \tilde{t}} = -\nabla^* \cdot [\tilde{\rho}^* \tilde{\boldsymbol{v}}^*] + \tilde{\lambda} \nabla^{*2}(\tilde{\rho}^*) + \tilde{\rho}^* \tilde{\beta}\big(\mathcal{D}^* - \langle \mathcal{D}^* \rangle\big), \tag{8}$$

where

$$\tilde{v}_i^* = \tilde{W}_{ij} n_j - \iota[\tilde{D}_{ij} n_j - n_i n_j n_k \tilde{D}_{jk}].$$

Richards et al. (2021) constrained the non-dimensional parameters $\tilde{\lambda}, \iota, \tilde{\beta}$ as functions of temperature. The parameters are constrained as:

$$\tilde{\lambda} = 3.04 \times 10^{-4} T + 0.161$$

$$\iota = 0.0259 T + 1.78 \tag{9}$$

$$\tilde{\beta} = 0.171 T + 5.90$$

where T is in °C. Equations (8) and (9) combined, when solved with the spectral method defined in Richards et al. (2021), represent the SpecCAF model.

3.2 Pole figure and cross section representation

To illustrate the model output and its representation, we show in Fig. 5 an example of model output obtained by solving the model at $T = -5°$ C, in simple shear ($\mathcal{W} = 1$). To visualise how the fabric changes with increasing strain, we plot slices of the pole figure at $y = 0$. The example pole figure in (a) is plotted at a strain of $\gamma = 0.5$. The value of ρ^* at $y = 0$ is plotted in (b) for each strain. This shows how the CPO develops from an isotropic fabric. A secondary cluster can clearly be seen as a transient feature which has mostly disappeared by $\gamma = 0.8$.

4 Results

4.1 General fabric evolution: dependence on temperature and vorticity number

We explore fabric evolution across a complete range of vorticity numbers $\mathcal{W}$ and temperatures T relevant to ice-sheet flow. To make comparisons, we will limit our analysis to fabrics undergoing a constant two-dimensional deformation and at a constant temperature. The vorticity number, defined in Eq. (1), gives the ratio of vorticity to strain-rate magnitude. However, it does not fully constrain the velocity gradient. We define the non-dimensional velocity gradient as:

$$\nabla \tilde{\boldsymbol{u}} = \frac{\sqrt{2}}{2} \begin{bmatrix} 1 & \mathcal{W} \\ -\mathcal{W} & -1 \end{bmatrix} \tag{10}$$

This gives pure shear for $\mathcal{W} = 0$, simple shear for $\mathcal{W} = 1$ and rigid-body rotation as $\mathcal{W} \to \infty$. and keeps the principal-axes of the strain-rate tensor $\tilde{\mathbf{D}}$ unchanged. Furthermore the pre-factor is chosen so the non-dimensional equivalent of the effective
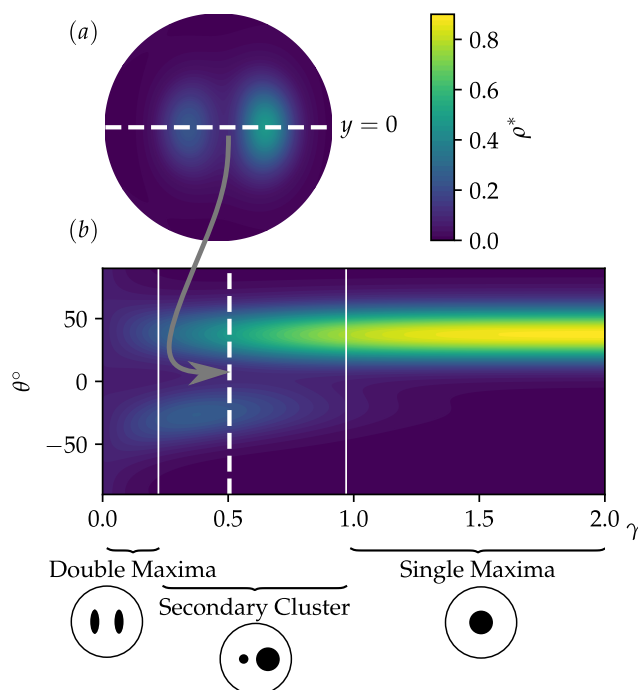
Figure 5. To illustrate the fabric we show a simulation in simple shear at $T = -5°$ C. (a) shows a pole figure from the model at $y = 0.5$. The white dotted line in (a) shows $y = 0$. (b) shows ρ^* at $y = 0$ against strain. Here the white dotted line highlights the strain at witch the pole figure is plotted. Also highlighted is the classification of the different fabric types at different strains; from double-maxima to secondary cluster to the steady state single maxima.

strain-rate is kept at unity:

$$\sqrt{\tilde{D}_{ij}\tilde{D}_{ij}} = 1. \tag{11}$$

With the velocity gradient fully defined, we explore the fabric dynamics produced across T-$\mathcal{W}$ space in Fig. 6. For each square we show the slice through the pole figure at $y = 0$ (explained in Fig. 5) up to a finite strain of $\gamma = 2$. The temperature range is from $-30°$ C to $-10°$ C, temperatures typical in ice sheets (Duval et al., 2010). The vorticity number ranges from $\mathcal{W} = 0.1$, very close to pure shear, and $\mathcal{W} = 10$ representing highly vortical flow with curved streamlines. This provides a detailed picture of how the fabric evolves with increasing strain, providing insights into deformations between compression and simple shear as well analysis of fabrics produced by deformations more rotational than simple shear. For low vorticity numbers, a single maximum can be seen at low temperatures which develops into double-maxima as strain increases. As $\mathcal{W}$ increases the clusters are moved by the rotational component of the deformation, resulting in a primary and secondary cluster. The weaker, secondary cluster is gradually consumed by migration recrystallization as strain increases, leading to a single maximum at high strains, for $\mathcal{W} \sim O(1)$.

205   We present in Fig. 6 analysis of fabrics produced in highly rotational ($\mathcal{W} > 1$) deformations, which as we have shown are prevalent in real-world conditions (figs. 3,4). Figure 6 shows that the fabric is strongest for $\mathcal{W} = 1$, and weakens as vorticity increases past this. For example, for $\mathcal{W} = 10$ there is only a very weak CPO produced. Furthermore at high vorticity numbers oscillation can be seen in the fabric pattern. To further analyse very high vorticity numbers we show the fabric produced as $\mathcal{W} \to \infty$ in Fig. 7. This fabric is seen for any vorticity number above $\mathcal{W} \approx 50$. The J index of this fabric is 1.12, very close

210   to completely isotropic ($J = 1$). It is unlikely this weak girdle fabric would be distinguishable from an isotropic fabric in a physical sample, where the CPO is determined by sampling a limited number of grain orientations.

4.2   Fabric regime diagrams for cluster angle and fabric type

To distil all the complex information shown in Fig. 6 and make this information more easily accessible, we analyse both the angle of the primary cluster and the regimes of different fabric patterns. The angle between the primary cluster and the

215   compression axis is shown in Fig. 8 at six separate finite strain values, across $\mathcal{W}$-T space. Even at a low finite strain of $\gamma = 0.3$ there is already an established difference in angle across the parameter space (Fig. 8a). Low temperatures and low vorticity numbers have the primary cluster most closely aligned with the compression axis. The angle then increases as both temperature and especially vorticity number increase. As strain increases the variation in angle increases. However, for a finite strain greater than 1 the angle is mostly invariant with strain. Across the strain and temperature range, an angle of around $40°$ implies simple

220   shear ($\mathcal{W} \approx 1$), whereas if the primary cluster and compression axis are coincident, this suggests pure shear at $T \approx -30°$ C .

As a means to visualise the variety of fabrics in terms of both the parameter space and across possible finite strains we show a regime diagram for fabric patterns in Fig. 9. To define whether a fabric is a double-maxima, secondary cluster or single-maxima we take the ratio of the two largest peaks in the fabric. If the 2nd largest peak is less than 10% the strength of the largest peak, it is defined as a single-maxima. If the strength of the 2nd largest peak is between 10% and 90% of the largest

225   peak, it is defined as a secondary cluster. If it is $> 90\%$ it is defined as a double-maxima. Contour lines of primary cluster angle at $20°$ and $50°$ are also shown. This shows the different fabric types (Fig. 1) across the space of temperature, vorticity number and finite strain. The figure is in the same format as 8.

Figure 9a shows the initial fabric after a finite strain of only $\gamma = 0.3$. There are three regimes at this finite strain. For approximately $\mathcal{W} < 1$ a double-maxima is produced. There is a small region, at high vorticity numbers and primarily at low

230   temperatures but extending into high temperatures, at which a single-maxima is produced. Otherwise a secondary cluster is produced, this occurs for relatively high vorticity numbers and is more dominant at higher temperatures, as expected. At higher finite strain the double-maxima pattern becomes less prevalent, only occurring at lower vorticity numbers or not at all. This highlights the transient nature of this pattern. As a reminder, the double-maxima is the 2D equivalent of a cone-shape fabric (Fig. 1). The double-maxima fabric is only present up to a finite strain of about $\gamma = 0.5$. In Fig. 9c, at $\gamma = 1.0$ the parameters

235   space is dominated by single-maxima and secondary cluster patterns. Ice fabrics which develop at higher temperatures are dominated by secondary cluster patterns, with the exception of around $\mathcal{W} \approx 3$, where a single-maxima occurs as the secondary cluster is too weak. At lower temperatures a single-maxima is produced as migration recrystallization is not active enough for multiple clusters to be produced. This balance between a single-maximum fabric and a secondary cluster fabric continues as

the finite strain increases, with a single-maxima also becoming more prevalent at lower vorticity numbers at the highest finite
240 strains (Fig. 9e and f).

To illustrate the difference in pole figure patterns at the same finite strain but different temperatures and deformations we plot pole figures at a finite strain of $\gamma = 2$ (Fig. 10) overlaid onto a regime diagram of fabric patterns. The pole figures are centred at the vorticity number and temperature they are simulated at. Figure 10 highlights fabrics are still variable despite being in the same regime. The fabric at $\mathcal{W} = 1, T = -5°$ C is much stronger than the fabric at $\mathcal{W} = 10, T = -30°$ C or $\mathcal{W} =$
245 $0.1, T = -30°$ C, however they are all single-maxima. We also note the difference in angle of the primary cluster across the parameter space: approximately $0°$ for $\mathcal{W} = 0.1, T = -30°$ C but increasing as $\mathcal{W}$ and T increase, as shown in Fig. 8.

4.3 Steady state fabric analysis

A variable that is central to the interpretation of ice core fabrics is the finite strain at which the fabric can be said to have reached its final steady state. Our predictions for the final steady state properties are shown in Fig. 11, across the space of $\mathcal{W}$-T. Here,
250 we define the steady state strain as being reached once the rolling average of the J index (Bunge, 1982), a measure of fabric concentration, defined as:

$$J = \int_{S^2} \rho^{*2} \, d\boldsymbol{n}. \tag{12}$$

over a finite strain window of 0.5 gets within 10% of the steady-state value. An example showing the evolution of the J index and the finite strain at which it reaches steady state is illustrated in Fig. 11c.
255 Figure 11a shows the finite strain at which steady-state is reached across the T-$\mathcal{W}$ space. At the highest temperatures and at vorticity numbers $\mathcal{W} \approx 0.02$ the highest finite strain is needed to reach a steady-state fabric, of around $\gamma = 14$. This occurs as the very small amount of rotation away from pure shear ($\mathcal{W} = 0$) causes a very slow transition from a double-maxima to a single-maxima, causing the J index to increase. For extremely low vorticity numbers ($\mathcal{W} \approx 0.01$) this change is so gradual that the fabric is defined as 'steady' earlier. Only $\mathcal{W} = 0$ has a stable double-maxima. This switch in steady-state strain is
260 not seen at low temperatures as migration recrystallization is not active enough to produce a double-maxima. For all fabrics explored between pure and simple shear ($0 < \mathcal{W} < 1$) a large finite strain is required to reach steady state of $\gamma > 1.3$. Fabrics reach steady state at the lowest finite strains at relatively high vorticity numbers of $\mathcal{W} \approx 4$. At higher vorticity numbers than this there is some oscillation in the fabric causing the steady-state strain to increase. Figure 11b shows the value of J at the steady state. Fabrics are strongest for $\mathcal{W} \approx 0.4$ and at higher temperatures, while for high $\mathcal{W}$, $J \approx 1$ i.e. an isotropic fabric, as
265 seen in Fig. 6. This figure highlights the effect even a small amount of rotation (i.e. $\mathcal{W} = 0.02$) has on the steady-state fabric, by making the double-maxima pattern seen in pure shear unstable.

5 Discussion

The analysis we have presented here covers the whole range of vorticity numbers and temperatures present in the natural world, a first for fabric modelling. In this paper we have limited the analysis to fabrics produced under constant deformation

270 and temperature. Although ice in the natural world will undergo changing deformations, our analysis is an important first step to provide insights into fabrics produced for deformations away from pure and simple shear. Furthermore, the fabrics analysed here are highly relevant for ice deformed in the laboratory, which is in most cases deformed at constant temperature and vorticity number.

5.1 Fabrics patterns across deformation and temperature space

275 Previous work has focused on modelling fabrics produced at fixed deformations (Llorens et al., 2016), or modelling the deformation experienced by ice at a divide (Bargmann et al., 2012). Due to the computational efficiency of our model, we have been able to perform many simulations across the parameter space of temperature and vorticity number to show how fabrics vary.

Our work generally shows a smooth transition between these two deformations, as can be seen in Fig. 6. As shown in Fig. 3 these deformations are important in the real-world and must be taken into account when considering ice fabrics, rather than

280 focusing on the isolated cases of pure and simple shear.

The weak fabric seen for highly rotational flows is novel. Throughout these deformations we have kept the magnitude of $\mathbf{D}$, the strain-rate tensor, constant. Therefore, at high vorticity numbers the weak fabric seen in figs. 6 and 7 is not caused by a lack of deformation. Instead it is due to the rotational component acting to quickly smear any cluster produced by basal-slip deformation or migration recrystallization to orientations where the cluster is consumed by migration recrystallization. The

285 end result as $\mathcal{W} \to \infty$ is a very weak girdle fabric with the girdle aligned to the axis of vorticity.

The regime diagram in 9 shows the fabric patterns produced across the space of vorticity number, temperature and strain. From experimentally deformed ice, the vast majority of fabrics produced are cone-shape fabrics (Fan et al., 2020). However, ice deformed in the laboratory in compression can only reach strains of up to $\gamma = 0.5$ and Fig. 9 highlights how double-maxima fabrics are only present up to these strains. Above $\gamma = 0.5$, secondary cluster and single-maxima patterns are more prevalent.

290 Importantly, secondary cluster fabrics, which have been to-date only seen in simple shear ($\mathcal{W} = 1$), can occur at very low vorticity numbers (Fig. 9c,d).

5.2 Finite strains required to reach steady-state fabrics

For the interpretation of ice fabrics it is essential that we know the strain at which fabrics reach steady-state. In this paper we have presented the first complete assessment of fabric timescales to steady state (Fig. 11). In compression, experiments can

295 only reach a maximum strain of $\gamma \approx 0.5$. It is often assumed that a strain of around $\gamma = 0.2$ represents a steady state in the mechanical properties, and consequently in fabric (Jacka, 2000). However, recent experiments show that the fabric continues to evolve past this (Piazolo et al., 2013; Qi et al., 2017). It is also known that fabrics require higher finite strain to reach steady-state in simple shear (Journaux et al., 2019). Qi et al. (2017) note that fabric data is required at higher strains than has been achieved to date by compression experiments to link to high-strain natural environments. The results in our paper fill this

300 missing gap. Figure 11 showing the steady-state strain and fabric strength, allows us to quantify when fabrics have reached steady state across the parameter space. For low $\mathcal{W}$, in experiments and in Fig. 6, a CPO quickly develops at very low strain $\gamma \approx 0.2$, (also seen in Craw et al., 2018). Although the fabric pattern does not change as strain increases, it cannot be said to be

in steady-state because the concentration of orientation at the clusters continues to increase. It should be noted that any change in fabric intensity will directly affect the mechanical properties such as the degree of viscous and seismic anisotropy (Duval

305   et al., 1983; Matsuoka et al., 2003).

Figure 11 shows that between pure and simple shear the strain at which a CPO reaches steady-state, for constant temperature and deformation is very high, always greater than $\gamma = 1.3$. From this we can make three remarks. Firstly, reaching a true steady state is impossible for experiments performed in compression: finite strains greater than $100\%(\gamma = 1)$ are required, higher than what is possible. However reaching steady state for simple shear experiments is possible, especially for ice deformed in

310   torsion such as by Journaux et al. (2019) where finite strains of $\gamma > 3$ (which is required to reach steady-state) are possible. Secondly, the steady-state strain is dependent on deformation and temperature, and varies by more than a factor of four across the space. Thirdly, in terms of steady-state properties, exactly pure shear ($\mathcal{W} = 0$) is a fairly special case: only with no rotational component in the fabric is a double-maxima (or cone-angle) fabric pattern stable as $\gamma \to \infty$. Deformations in the natural world will always have some rotational component but the majority of fabrics deformed in the laboratory have been deformed in this

315   special case of $\mathcal{W} = 0$.

5.3   Consequences for ice core interpretation

Analysis and interpretation of ice cores remain key for understanding the processes occurring in the natural world, for both understanding the past climate history as well as understanding ice sheet dynamics (Faria et al., 2014). The regime diagrams we have constructed (figs. 8,9) can be used as a toolkit to interpret ice cores. For example a single maxima fabric with an

320   angle of $20°$ between the compression axis and primary cluster centre implies the core has undergone mostly compression at low temperature. If other constraints are available, the dominant deformation and temperature can be further constrained. As our work here is for constant temperature and vorticity number, any ice core fabric interpretation will inherently assume that an ice core that has been deformed primarily at a dominant temperature and deformation over its recent history. Since temperature varies with depth in an ice sheet (Paterson, 1999), this method is likely to be most reliable for ice cores where the

325   ice is primarily moving horizontally i.e. away from ice divides. We also assume an initial random orientation for the fabric. Although deformation history in the natural world is likely to be complex, this is a reasonable assumption because ice formed from surface accumulation will initially have a random distribution of orientations (Montagnat et al., 2020).

The fabric pattern is a robust way to interpret ice cores, as it requires no assumptions about the deformation direction. The regime diagram in Fig. 9 which is based on the fabric pattern only is complex but insights can be drawn nonetheless.

330   For example, the presence of double-maxima fabrics (two equal strength clusters) implies that the fabric has undergone a relatively low strain. A secondary cluster fabric implies that the fabric is likely to be at intermediate strains, and at temperatures $T > -20°$ C. A very weak secondary cluster fabric implies a highly rotational deformation $W > 3$.

If other information about the fabric history is known, figs. 8 and 9 can be used in combination to extend this knowledge. For example, if there are independent constraints on the orientation of the deformation axis, then the angle of the primary cluster

335   can be used to interpret ice cores as well. As can be seen in Fig. 8 the angle of the primary cluster is relatively invariant with

strain. Knowing this angle can therefore give a good estimate of the vorticity number and temperature, for deformations which are primarily 2D.

5.4 Implications for ice flow properties and modelling

Viscous anisotropy of ice is controlled by the fabric and is a key control of the flow field (e.g. Minchew et al., 2018). This anisotropy is dependent on the pattern, direction and strength of the fabric. The current approach common in ice-sheet models is to represent anisotropy with an enhancement factor which scales the viscosity, either globally (Graham et al., 2018) or locally (Placidi et al., 2010). The model SpecCAF used in our paper can be coupled with an anisotropic viscosity formulation to include directional variation in viscosity. This has been done with simplified fabric evolution models which do not include recrystallization and temperature dependence (Martín et al., 2009). The high sensitivity of fabric strength and patterns to temperature shown in our paper and in experimental work (Qi et al., 2019) implies the potential for anisotropy to generate interesting flow features. This can only be captured with a coupled fabric model including a temperature dependent fabric. Temperature can also affect the flow through viscous heating (e.g Hindmarsh, 2004) and a temperature dependent fabric model coupled to anisotropic viscosity such as Gillet-Chaulet et al. (2005) would allow us to understand what proportion of the effects of temperature are a consequence of viscous heating and what proportion arise through temperature induced changes to the fabric.

The fabrics we have shown here give insight into where anisotropy may be most important in an ice sheet. Areas with strong fabrics will be highly anisotropic, with the viscosity varying in different directions. Anisotropic flow is not well studied but initial simulations with coupled anisotropic flow show it can explain hitherto unexplained observations such as syncline patterns observed under ice divides (Martín et al., 2009). Our analysis of fabrics produced in highly rotational deformations showing an almost isotropic fabric (as seen in figs. 6 and 11b) implies that in the regions of Antarctica where the flow is highly rotational, which as we can see in Fig. 3 does occur, the fabric will evolve towards a state with limited anisotropy (directional variation in viscosity). However areas of approximately simple shear ($\mathcal{W} = 1$) show the strongest fabrics and hence the strongest effect of anisotropy. As we have shown in fig 4 this kind of deformation is the most common in Antarctica. This means viscous anisotropic affects are widespread, further motivating the need to fully represent them in models. In future work it would also be possible to explore how seismic wave velocities vary with the different fabrics modelled in this paper, again comparing to real world observations.

6 Conclusions

Prediction of fabric evolution is pivotal for the correct interpretation of ice core fabrics and reliably predicting ice losses in a changing climate using ice sheet modelling. Our work extends the ability to predict fabric evolution from the end member deformation regimes of pure and simple shear to general and rotational flow. As such the presented study represents an important step towards understanding fabrics in fully general conditions which is key for understanding viscous anisotropy and therefore large scale ice sheet flow modelling. We have shown that deformations outside of pure and simple shear are important

in natural ice flows such as Antarctica. Furthermore ice flow regimes more rotational than simple shear are not only possible but common in regions such as shear margins and ice streams which are of significant interest (e.g Meyer and Minchew, 2018; Stoll, 2019). There is the potential for future work to extend the modelled fabrics to calculate to seismic anisotropic properties, enabling us to further improve our understanding of ice in natural flows.

The regime diagrams presented are a useful tool to help with the interpretation of ice core data. In combination with other information, such as the plane of deformation or an estimate of the temperature at which a core was deformed at, these regime diagrams can be used to determine the primary deformation and temperature undergone by an ice core.

Highly rotational deformations were investigated for the first time and showed a weak girdle fabric aligned to the axis of vorticity. We have also highlighted how between pure and simple shear true steady states, where both the fabric pattern and fabric intensity are unchanging, are only reached at finite strains of at least $\gamma = 1.3$. This could only be achieved in the laboratory by simple shear experiments, such as by Journaux et al. (2019). These strains cannot be achieved in compression experiments. Furthermore the steady-state properties of pure shear fabrics are different from those with even a very small amount of rotation.

The understanding we provide of ice fabrics under a wider range of deformations, which will be seen in the natural world, provides insights into how and where viscous anisotropy will be important for ice flow dynamics. Intermediate deformations between pure and simple shear produce the strongest CPOs, suggesting anisotropy will be most important in these regions. Similarly, as highly rotational deformations produce a weak fabric, there is likely to be a less dominant affect of anisotropy in such regions. Our understanding of these issues could be further improved by combining our model with an anisotropic viscosity formulation to model the coupled fully anisotropic flow of ice necessary to predict ice flow in a changing climate.

Code availability. A python implementation of SpecCAF, alongside code to reproduce the figures in the Results section, is available at http://doi.org/10.5281/zenodo.4670218

Author contributions. All authors designed the research and edited the manuscript. DR developed the model code, performed the analysis and visualization and wrote the draft.

Competing interests. The authors declare that they have no conflict of interest.

References

395 Azuma, N. and Higashi, A.: Mechanical Properties of Dye 3 Greenland Deep Ice Cores, Annals of Glaciology, 5, 1–8, https://doi.org/10.3189/1984AoG5-1-1-8, 1984.

Bailey, C. M. and Eyster, E. L.: General shear deformation in the Pinaleño Mountains metamorphic core complex, Arizona, Journal of Structural Geology, 25, 1883–1892, https://doi.org/10.1016/S0191-8141(03)00044-0, 2003.

Bargmann, S., Seddik, H., and Greve, R.: Computational modeling of flow-induced anisotropy of polar ice for the EDML deep drilling
400 site, Antarctica: The effect of rotation recrystallization and grain boundary migration, International Journal for Numerical and Analytical Methods in Geomechanics, 36, 892–917, https://doi.org/10.1002/nag.1034, 2012.

Beam, E. C. and Fisher, D. M.: An estimate of kinematic vorticity from rotated elongate porphyroblasts, Journal of Structural Geology, 21, 1553–1559, https://doi.org/10.1016/S0191-8141(99)00110-8, 1999.

Booth, A. D., Christoffersen, P., Schoonman, C., Clarke, A., Hubbard, B., Law, R., Doyle, S. H., Chudley, T. R., and Chalari, A.: Distributed
405 Acoustic Sensing of Seismic Properties in a Borehole Drilled on a Fast-Flowing Greenlandic Outlet Glacier, Geophysical Research Letters, 47, e2020GL088 148, https://doi.org/10.1029/2020GL088148, publisher: John Wiley & Sons, Ltd, 2020.

Bunge, H.: Texture Analysis in Materials Science: Mathematical Models, Butterworths, London, 1982.

Craw, L., Qi, C., Prior, D. J., Goldsby, D. L., and Kim, D.: Mechanics and microstructure of deformed natural anisotropic ice, Journal of Structural Geology, 115, 152–166, https://doi.org/10.1016/j.jsg.2018.07.014, 2018.

410 Drury, M. and Urai, J.: Deformation-related recrystallization process, Tectonophysics, 172, 235–253, https://doi.org/10.1016/0040-1951(90)90033-5, 1990.

Duval, P., Ashby, M. F., and Anderman, I.: Rate-controlling processes in the creep of polycrystalline ice, The Journal of Physical Chemistry, 87, 4066–4074, https://doi.org/10.1021/j100244a014, 1983.

Duval, P., Montagnat, M., Grennerat, F., Weiss, J., Meyssonnier, J., and Philip, A.: Creep and plasticity of glacier ice: a material science
415 perspective, Journal of Glaciology, 56, 1059–1068, https://doi.org/10.3189/002214311796406185, 2010.

Fan, S., Hager, T., Prior, D. J., Cross, A. J., Goldsby, D. L., Qi, C., Negrini, M., and Wheeler, J.: Temperature and strain controls on ice deformation mechanisms: insights from the microstructures of samples deformed to progressively higher strains at $-$10, $-$20 and $-$30\,$^{\circ}$C, The Cryosphere Discuss., 2020, 1–43, https://doi.org/10.5194/tc-2020-2, 2020.

Faria, S. H., Weikusat, I., and Azuma, N.: The microstructure of polar ice. Part I: Highlights from ice core research, Microdynamics of Ice,
420 61, 2–20, https://doi.org/10.1016/j.jsg.2013.09.010, 2014.

Fossen, H. and Tikoff, B.: The deformation matrix for simultaneous simple shearing, pure shearing and volume change, and its application to transpression-transtension tectonics, The Geometry of Naturally Deformed Rocks, 15, 413–422, https://doi.org/10.1016/0191-8141(93)90137-Y, 1993.

Fujita, S., Maeno, H., and Matsuoka, K.: Radio-wave depolarization and scattering within ice sheets: a matrix-based model to link radar and
425 ice-core measurements and its application, Journal of Glaciology, 52, 407–424, https://doi.org/10.3189/172756506781828548, edition: 2017/09/08 Publisher: Cambridge University Press, 2006.

Gagliardini, O., Zwinger, T., Gillet-Chaulet, F., Durand, G., Favier, L., de Fleurian, B., Greve, R., Malinen, M., Martín, C., R\a aback, P., Ruokolainen, J., Sacchettini, M., Schäfer, M., Seddik, H., and Thies, J.: Capabilities and performance of Elmer/Ice, a new-generation ice sheet model, Geoscientific Model Development, 6, 1299–1318, https://doi.org/10.5194/gmd-6-1299-2013, 2013.

430 Gillet-Chaulet, F., Gagliardini, O., Meyssonnier, J., Montagnat, M., and Castelnau, O.: A user-friendly anisotropic flow law for ice-sheet modeling, Journal of Glaciology, 51, 3–14, https://doi.org/10.3189/172756505781829584, 2005.

Gow, A. J.: Deep core studies of the accumulation and densification of snow at Byrd Station and Little America V, Antarctica, CRREL Research Report, 1961.

Graham, F. S., Morlighem, M., Warner, R. C., and Treverrow, A.: Implementing an empirical scalar constitutive relation for ice with flow-

435   induced polycrystalline anisotropy in large-scale ice sheet models, The Cryosphere, 12, 1047–1067, https://doi.org/10.5194/tc-12-1047-2018, 2018.

Gödert, G.: A mesoscopic approach for modelling texture evolution of polar ice including recrystallization phenomena, Annals of Glaciology, 37, 23–28, https://doi.org/10.3189/172756403781815375, 2003.

Hindmarsh, R. C. A.: Thermoviscous stability of ice-sheet flows, Journal of Fluid Mechanics, 502, 17–40,

440   https://doi.org/10.1017/S0022112003007390, 2004.

Holtzscherer, J. J., G. de Q. Robin, and Glen, J. W.: Depth of Polar Ice Caps, The Geographical Journal, 120, 193–202, https://doi.org/10.2307/1791535, publisher: [Wiley, Royal Geographical Society (with the Institute of British Geographers)], 1954.

Jacka, T. and Maccagnan, M.: Ice crystallographic and strain rate changes with strain in compression and extension, Cold Regions Science and Technology, 8, 269–286, https://doi.org/10.1016/0165-232X(84)90058-2, 1984.

445 Jacka, T. H.: Flow rates and crystal orientation fabrics in compression of polycrystalline ice at low temperatures and stresses, Physics of Ice Core Record, 2000.

Jiang, D.: Vorticity determination, distribution, partitioning and the heterogeneity and non-steadiness of natural deformations, Journal of Structural Geology, 16, 121–130, https://doi.org/10.1016/0191-8141(94)90023-X, 1994.

Johnsen, S. J., Dahl-Jensen, D., Dansgaard, W., and Gundestrup, N.: Greenland palaeotemperatures derived from GRIP bore hole temperature

450   and ice core isotope profiles, Tellus B: Chemical and Physical Meteorology, 47, 624–629, https://doi.org/10.3402/tellusb.v47i5.16077, publisher: Taylor & Francis, 1995.

Jordan, T. M., Schroeder, D. M., Elsworth, C. W., and Siegfried, M. R.: Estimation of ice fabric within Whillans Ice Stream using polarimetric phase-sensitive radar sounding, Annals of Glaciology, 61, 74–83, https://doi.org/10.1017/aog.2020.6, edition: 2020/02/03 Publisher: Cambridge University Press, 2020.

455 Journaux, B., Chauve, T., Montagnat, M., Tommasi, A., Barou, F., Mainprice, D., and Gest, L.: Recrystallization processes, microstructure and crystallographic preferred orientation evolution in polycrystalline ice during high-temperature simple shear, The Cryosphere, 13, 1495–1511, https://doi.org/10.5194/tc-13-1495-2019, 2019.

Kennedy, J. H. and Pettit, E. C.: The response of fabric variations to simple shear and migration recrystallization, Journal of Glaciology, 61, 537–550, https://doi.org/10.3189/2015JoG14J156, 2015.

460 Kluskiewicz, D., WADDINGTON, E., Anandakrishnan, S., Voigt, D., Matsuoka, K., and McCARTHY, M.: Sonic methods for measuring crystal orientation fabric in ice, and results from the West Antarctic ice sheet (WAIS) Divide, Journal of Glaciology, 63, 1–15, https://doi.org/10.1017/jog.2017.20, 2017.

Llorens, M.-G., Griera, A., Bons, P. D., Lebensohn, R. A., Evans, L. A., Jansen, D., and Weikusat, I.: Full-field predictions of ice dynamic recrystallisation under simple shear conditions, Earth and Planetary Science Letters, 450, 233–242,

465   https://doi.org/10.1016/j.epsl.2016.06.045, 2016.

Martín, C., Gudmundsson, G. H., Pritchard, H. D., and Gagliardini, O.: On the effects of anisotropic rheology on ice flow, internal structure, and the age-depth relationship at ice divides, Journal of Geophysical Research: Earth Surface, 114, https://doi.org/10.1029/2008JF001204, publisher: John Wiley & Sons, Ltd, 2009.

Matsuoka, K., Furukawa, T., Fujita, S., Maeno, H., Uratsuka, S., Naruse, R., and Watanabe, O.: Crystal orientation fabrics within the Antarctic
470 ice sheet revealed by a multipolarization plane and dual-frequency radar survey, Journal of Geophysical Research: Solid Earth, 108, https://doi.org/10.1029/2003JB002425, publisher: John Wiley & Sons, Ltd, 2003.

Meyer, C. R. and Minchew, B. M.: Temperate ice in the shear margins of the Antarctic Ice Sheet: Controlling processes and preliminary locations, Earth and Planetary Science Letters, 498, 17–26, https://doi.org/10.1016/j.epsl.2018.06.028, 2018.

Minchew, B., Meyer, C., Robel, A., Gudmundsson, G., and Simons, M.: Processes controlling the downstream evolution of
475 ice rheology in glacier shear margins: case study on Rutford Ice Stream, West Antarctica, Journal of Glaciology, 64, 1–12, https://doi.org/10.1017/jog.2018.47, 2018.

Montagnat, M., Löwe, H., Calonne, N., Schneebeli, M., Matzl, M., and Jaggi, M.: On the Birth of Structural and Crystallographic Fabric Signals in Polar Snow: A Case Study From the EastGRIP Snowpack, Frontiers in Earth Science, 8, 365, https://doi.org/10.3389/feart.2020.00365, 2020.

480 Mouginot, J., Rignot, E., and Scheuchl, B.: Continent-Wide, Interferometric SAR Phase, Mapping of Antarctic Ice Velocity, Geophysical Research Letters, 46, 9710–9718, https://doi.org/10.1029/2019GL083826, publisher: John Wiley & Sons, Ltd, 2019.

Passchier, C.: The classification of dilatant flow types, Journal of Structural Geology, 13, 101–104, https://doi.org/10.1016/0191-8141(91)90105-R, 1991.

Paterson, W. S. B.: The Physics of Glaciers, Pergamon, Oxford, 3rd edn., 1999.

485 Piazolo, S., Bons, P., and Passchier, C.: The influence of matrix rheology and vorticity on fabric development of populations of rigid objects during plane strain deformation, Tectonophysics, 351, 315–329, https://doi.org/10.1016/S0040-1951(02)00220-2, 2002.

Piazolo, S., Jessell, M. W., Prior, D. J., and Bons, P. D.: The integration of experimental in-situ EBSD observations and numerical simulations: a novel technique of microstructural process analysis, Journal of Microscopy, 213, 273–284, https://doi.org/10.1111/j.0022-2720.2004.01304.x, publisher: John Wiley & Sons, Ltd, 2004.

490 Piazolo, S., Wilson, C. J. L., Luzin, V., Brouzet, C., and Peternell, M.: Dynamics of ice mass deformation: Linking processes to rheology, texture, and microstructure, Geochemistry, Geophysics, Geosystems, 14, 4185–4194, https://doi.org/10.1002/ggge.20246, 2013.

Pimienta, P. and Duval, P.: Mechanical behavior of anisotropic polar ice, The Physical Basis of Ice Sheet Modelling, 170, 1987.

Placidi, L., Greve, R., Seddik, H., and Faria, S. H.: Continuum-mechanical, Anisotropic Flow model for polar ice masses, based on an anisotropic Flow Enhancement factor, Continuum Mechanics and Thermodynamics, 22, 221–237, https://doi.org/10.1007/s00161-009-
495 0126-0, 2010.

Qi, C., Goldsby, D. L., and Prior, D. J.: The down-stress transition from cluster to cone fabrics in experimentally deformed ice, Earth and Planetary Science Letters, 471, 136–147, https://doi.org/10.1016/j.epsl.2017.05.008, 2017.

Qi, C., Prior, D. J., Craw, L., Fan, S., Llorens, M.-G., Griera, A., Negrini, M., Bons, P. D., and Goldsby, D. L.: Crystallographic preferred orientations of ice deformed in direct-shear experiments at low temperatures, The Cryosphere, 13, 351–371, https://doi.org/10.5194/tc-
500 13-351-2019, 2019.

Richards, D. H., Pegler, S. S., Piazolo, S., and Harlen, O. G.: The evolution of ice fabrics: A continuum modelling approach validated against laboratory experiments, Earth and Planetary Science Letters, 556, 116 718, https://doi.org/10.1016/j.epsl.2020.116718, 2021.

Rongen, M., Bay, R. C., and Blot, S.: Observation of an optical anisotropy in the deep glacial ice at the geographic South Pole using a laser dust logger, The Cryosphere, 14, 2537–2543, https://doi.org/10.5194/tc-14-2537-2020, publisher: Copernicus Publications, 2020.

505 Shepherd, A., Ivins, E., Rignot, E., Smith, B., van den Broeke, M., Velicogna, I., Whitehouse, P., Briggs, K., Joughin, I., Krinner, G., Nowicki, S., Payne, T., Scambos, T., Schlegel, N., A, G., Agosta, C., Ahlstrøm, A., Babonis, G., Barletta, V., Blazquez, A., Bonin, J., Csatho, B., Cullather, R., Felikson, D., Fettweis, X., Forsberg, R., Gallee, H., Gardner, A., Gilbert, L., Groh, A., Gunter, B., Hanna, E., Harig, C., Helm, V., Horvath, A., Horwath, M., Khan, S., Kjeldsen, K. K., Konrad, H., Langen, P., Lecavalier, B., Loomis, B., Luthcke, S., McMillan, M., Melini, D., Mernild, S., Mohajerani, Y., Moore, P., Mouginot, J., Moyano, G., Muir, A., Nagler, T., Nield, G., Nilsson, J.,
510 Noel, B., Otosaka, I., Pattle, M. E., Peltier, W. R., Pie, N., Rietbroek, R., Rott, H., Sandberg-Sørensen, L., Sasgen, I., Save, H., Scheuchl, B., Schrama, E., Schröder, L., Seo, K.-W., Simonsen, S., Slater, T., Spada, G., Sutterley, T., Talpe, M., Tarasov, L., van de Berg, W. J., van der Wal, W., van Wessem, M., Vishwakarma, B. D., Wiese, D., Wouters, B., and The IMBIE team: Mass balance of the Antarctic Ice Sheet from 1992 to 2017, Nature, 558, 219–222, https://doi.org/10.1038/s41586-018-0179-y, 2018.

Stoll, N.: A first glimpse into the EGRIP ice core: An analysis of the influence of deformation and recrystallisation on fabric and microstruc-
515 tures of the Northeast Greenland Ice Stream, 2019.

Svendsen, B. and Hutter, K.: A continuum approach for modelling induced anisotropy in glaciers and ice sheets, Annals of Glaciology, 23, 262–269, https://doi.org/10.3189/S0260305500013525, 1996.

ten Grotenhuis, S. M., Piazolo, S., Pakula, T., Passchier, C. W., and Bons, P. D.: Are polymers suitable rock analogs?, Tectonophysics, 350, 35–47, https://doi.org/10.1016/S0040-1951(02)00080-X, 2002.

520 Tikoff, B. and Fossen, H.: The limitations of three-dimensional kinematic vorticity analysis, Journal of Structural Geology, 17, 1771–1784, https://doi.org/10.1016/0191-8141(95)00069-P, 1995.

Treverrow, A., Warner, R. C., Budd, W. F., and Craven, M.: Meteoric and marine ice crystal orientation fabrics from the Amery Ice Shelf, East Antarctica, Journal of Glaciology, 56, 877–890, https://doi.org/10.3189/002214310794457353, 2010.

van der Veen, C. and Whillans, I.: Development of fabric in ice, Cold Regions Science and Technology, 22, 171–195,
525 https://doi.org/10.1016/0165-232X(94)90027-2, 1994.

Wilson, C. J. and Peternell, M.: Ice deformed in compression and simple shear: control of temperature and initial fabric, Journal of Glaciology, 58, 11–22, https://doi.org/10.3189/2012JoG11J065, 2012.

Xypolias, P.: Vorticity analysis in shear zones: A review of methods and applications, Structural Diagenesis, 32, 2072–2092, https://doi.org/10.1016/j.jsg.2010.08.009, 2010.
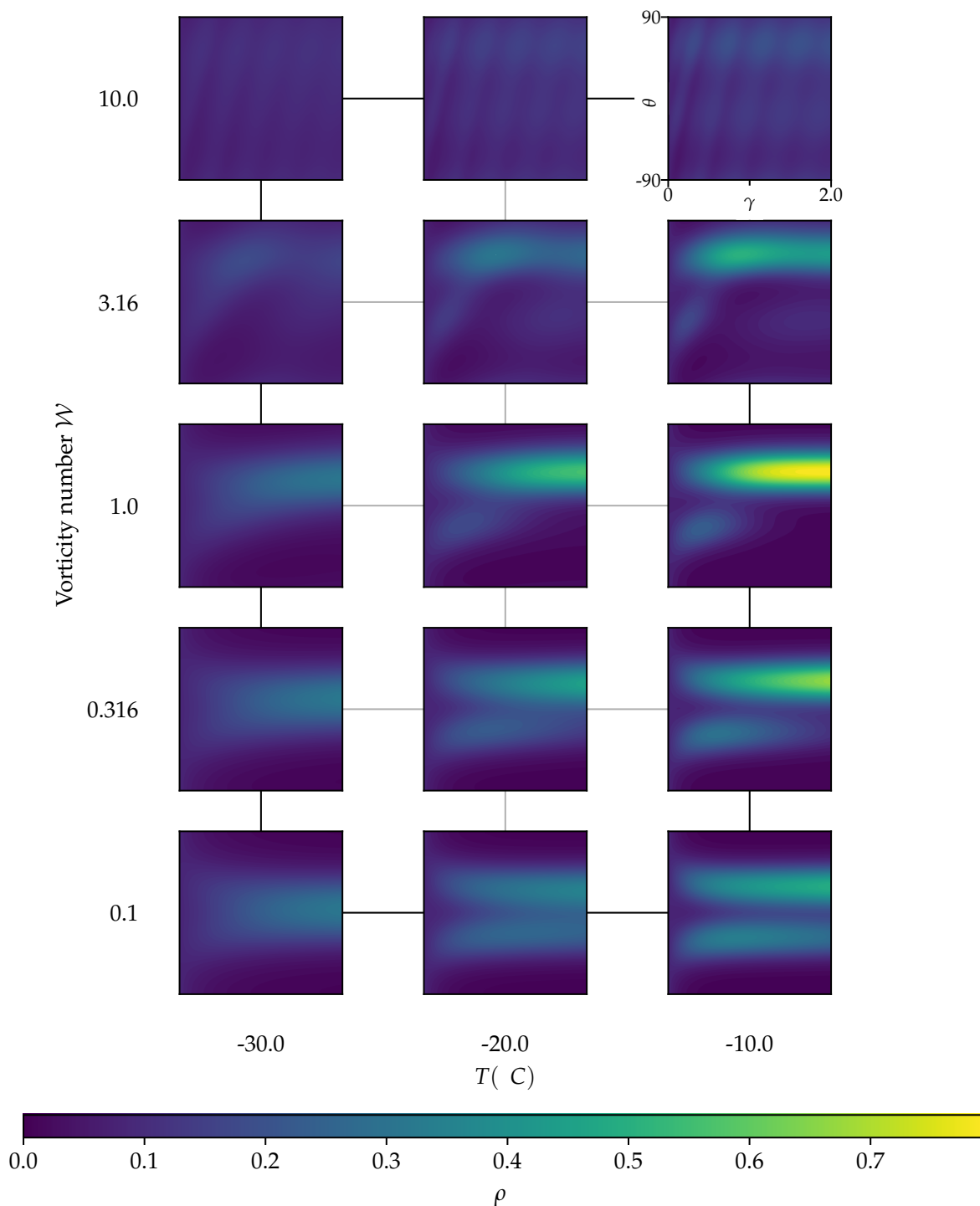
Figure 6. Slices of the pole figure showing the value of ρ^* at $y = 0$ for an array of temperatures and vorticity numbers. All $y = 0$ plots go to a strain of $\gamma = 2$. The colour limits are the same for all plots.
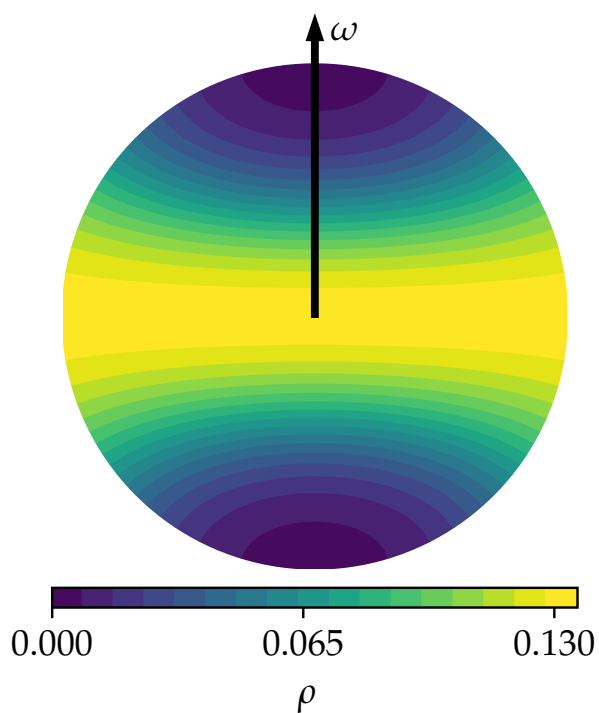
Figure 7. Pole figure for $\mathcal{W} \to \infty$ and $T = -5°$ C at steady-state. A very weak girdle fabric is produced, with the girdle coincident with the axis of vorticity, shown. This CPO has a J index of 1.196, where $J = 1$ is an isotropic fabric.
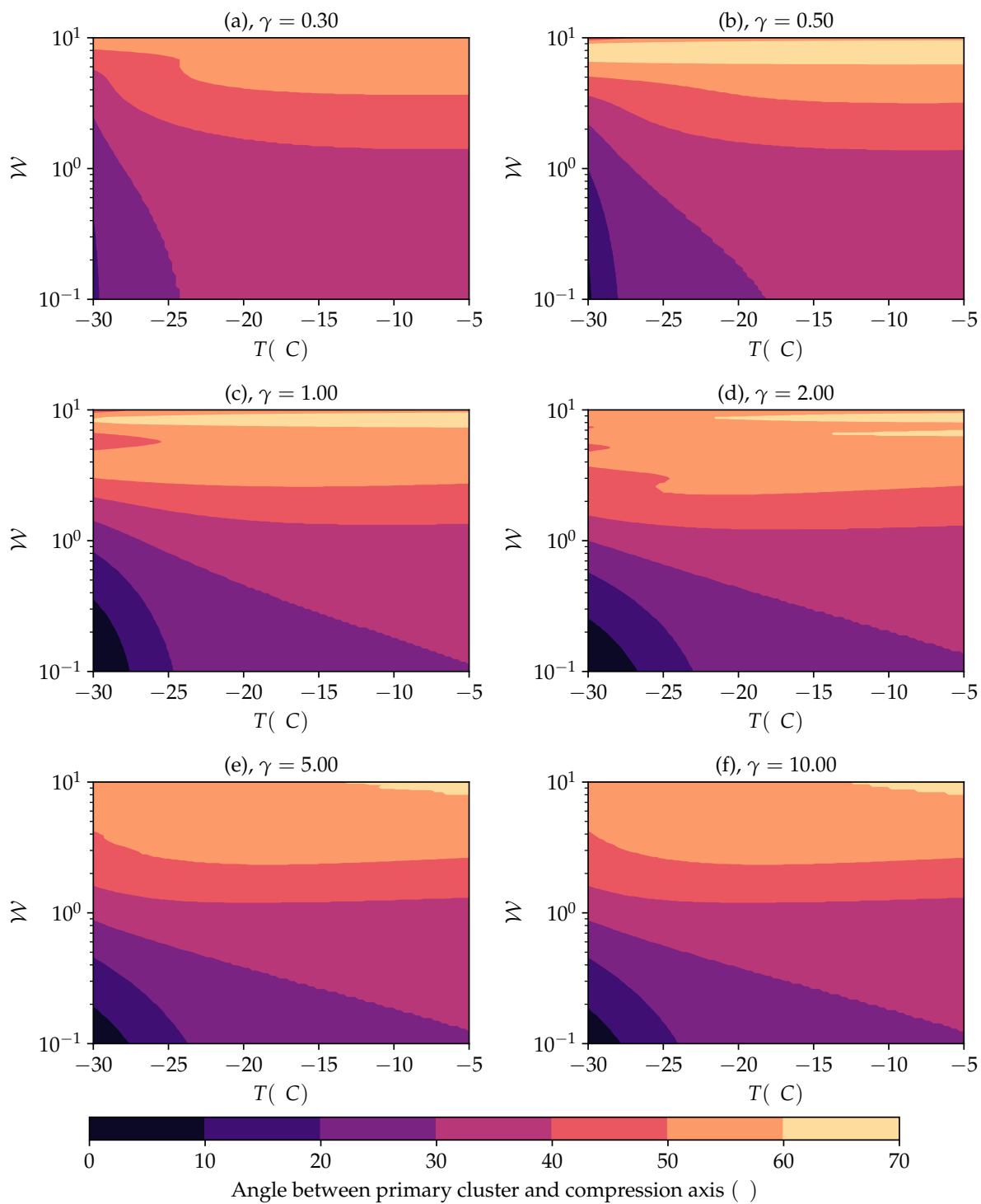
Figure 8. Diagram showing the angle (in degrees) of the largest cluster from the compression axis. Panels are shown for progressively increasing finite strain values. This angle is fairly invariant with finite strain.
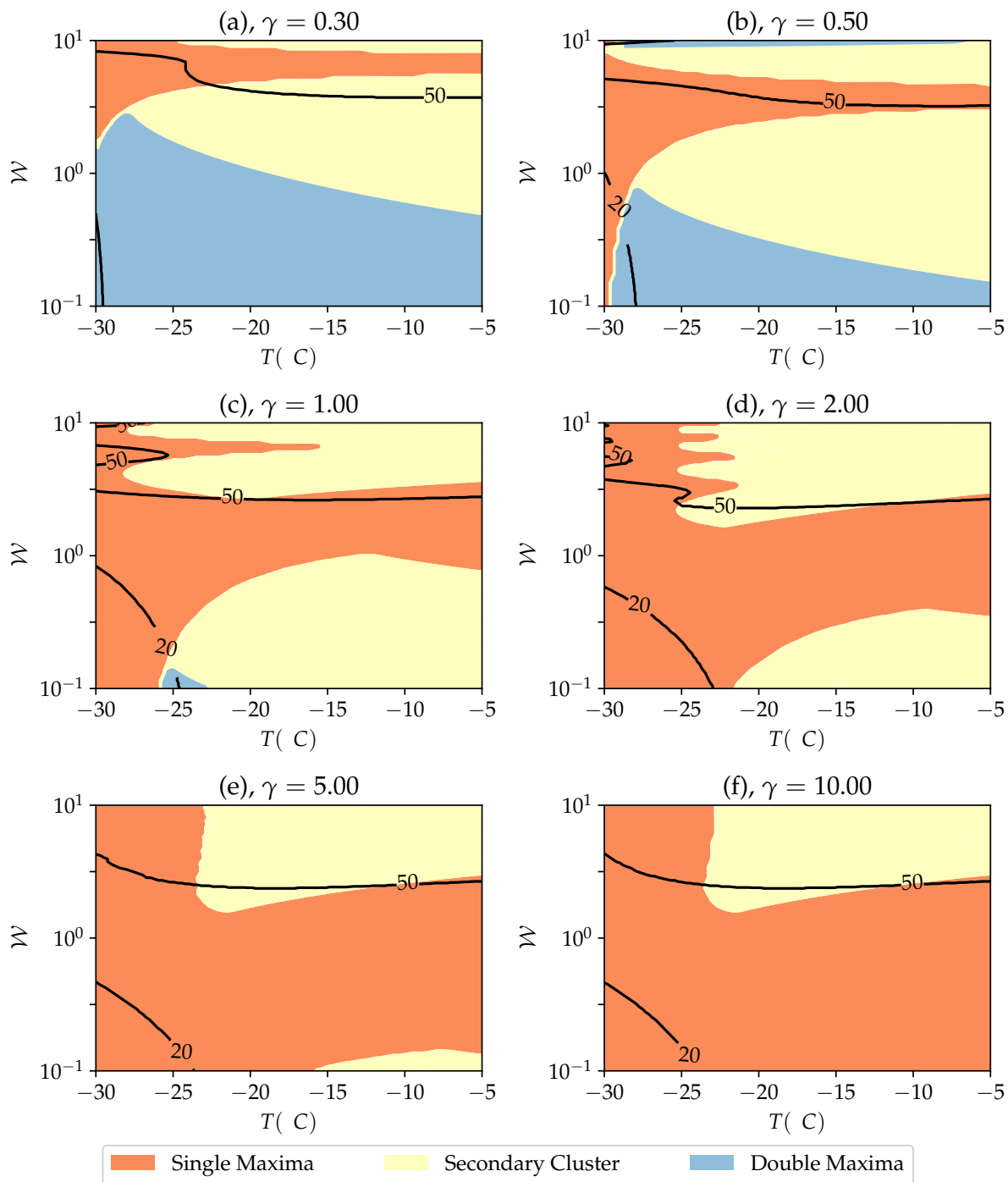
Figure 9. Regime diagram of the different fabric patterns which occur (defined in Fig. 1). The angle of the primary cluster in Fig. 8 at $20°$ and $50°$ is also overlaid. As in Fig. 8 diagrams are shown for discrete strain values.
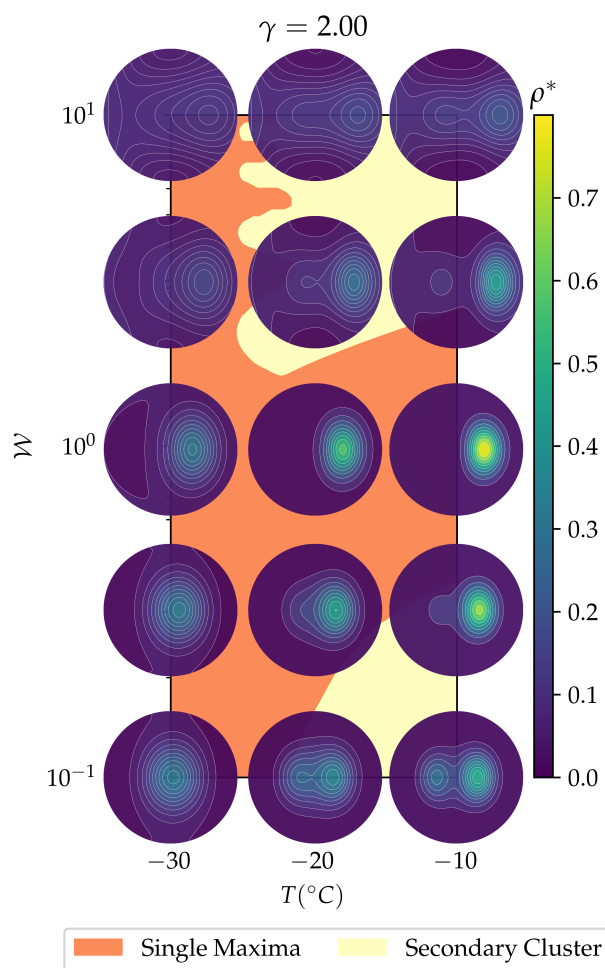
Figure 10. Pole figures overlaid onto the regimes at $\gamma = 2$. The pole figures are centred at the vorticity number and temperature they occur.
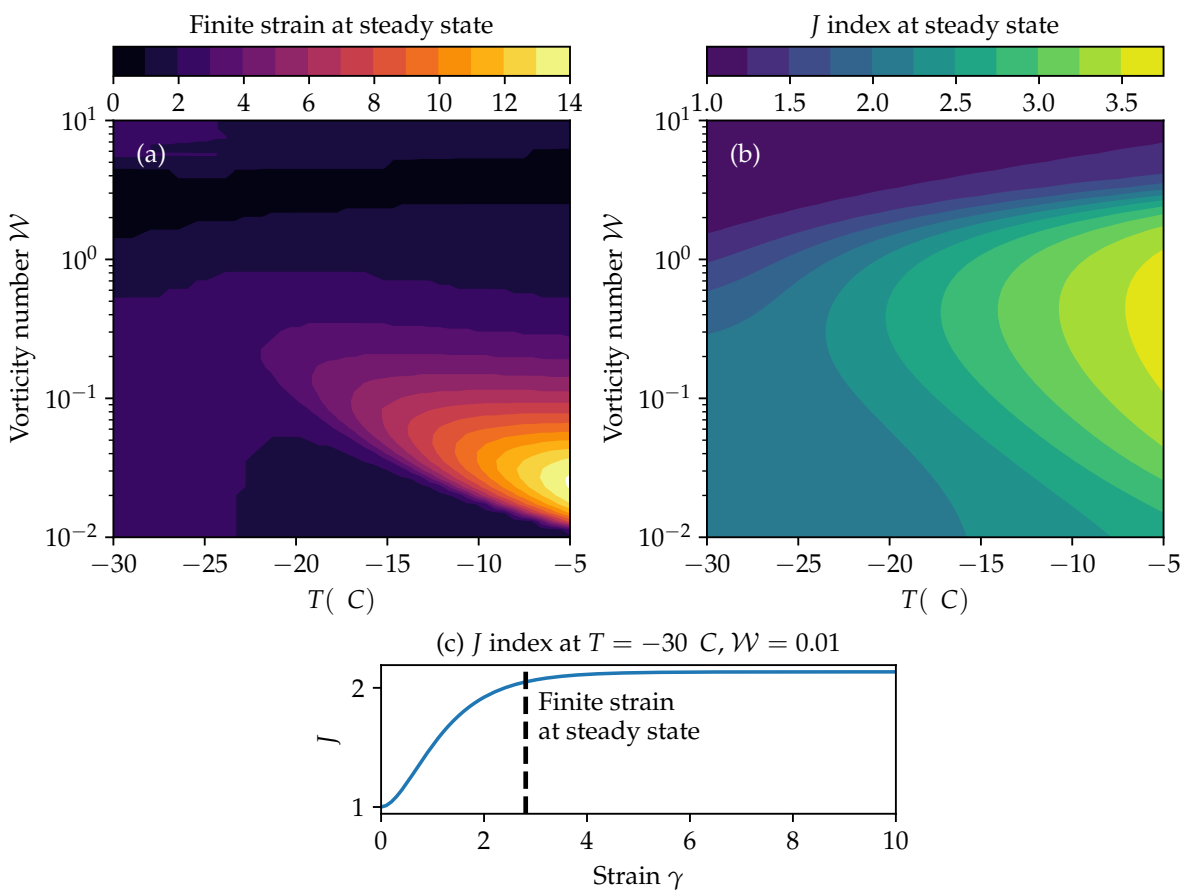
Figure 11. This figure shows information about the steady-state fabric. (a) shows the strain at which the fabric, at constant T and $\mathcal{W}$, reaches steady-state (defined as a rolling average of the J index over a strain window of 2 gets within 5% of the steady-state value). (b) shows the J index at the steady state. (c) shows the plot of J against strain γ at $T = -30°$ C, $\mathcal{W} = 0.01$, with the calculated steady-state strain